Smart Agricultural Technology 14 (2026) 102105

Contents lists available at ScienceDirect

Smart Agricultural Technology

journal homepage: www.journals.elsevier.com/smart-agricultural-technology

An open-architecture precision vertical farming system for sesame microgreens: Audit-ready telemetry for dynamic lighting and energy–biomass benchmarking

Marlus Dias Silva [a,*], Jaqueline Martins Vasconcelos [a], Fábia Barbosa da Silva [a], Adriano Soares de Oliveira Bailão [b], Ítalo Moraes Rocha Guedes [c], Márcio da Silva Vilela [d], Adriano Carvalho Costa [a], Márcio Rosa [e], Lucas Loram Lourenço [a], Fabiano Guimarães Silva [a,*]

[a] Laboratory of Advanced Studies in Vertical Farming, Federal Institute of Education, Science and Technology Goiano (IF Goiano), Rio Verde Campus, Rio Verde, Goiás, Brazil
[b] Laboratory of Computational Intelligence, Federal Institute of Education, Science and Technology Goiano (IF Goiano), Rio Verde Campus, Rio Verde, Goiás, Brazil
[c] Brazilian Agricultural Research Corporation (EMBRAPA), Embrapa Vegetables (Embrapa Hortaliças), Brasília, Federal District, Brazil
[d] Laboratory of Automation, Simulation and Control, Federal Institute of Education, Science and Technology Goiano (IF Goiano), Rio Verde Campus, Rio Verde, Goiás, Brazil
[e] Graduate Program in Plant Production, University of Rio Verde (UniRV), Rio Verde, Goiás, Brazil

ARTICLE INFO

Keywords:
Precision vertical farming
Plant factory with artificial lighting (PFAL)
Internet of things (IoT)
Dynamic lighting
Energy use efficiency
Sesame microgreens
Reproducibility

ABSTRACT

The reproducibility of lighting protocols in *Plant Factories with Artificial Lighting* (PFALs) is frequently constrained by the scarcity of auditable operational data. This study presents and validates an open-architecture *Precision Vertical Farming System* (PVFS) capable of executing dynamic photosynthetic photon flux density (PPFD) profiles under controlled Daily Light Integral (DLI), ensuring traceability via IoT telemetry. The system was applied to sesame microgreens grown using a 2×4 factorial design, combining temporal profiles (Constant vs. Gaussian) and light spectra (White, Blue, Red, and RBW), with DLI equalized at $10.8\,\mathrm{mol\,m^{-2}\,d^{-1}}$. Telemetric validation demonstrated high stability (jitter ≈ 0) and data completeness ($> 98\%$), enabling the precise calculation of Specific Energy Consumption (SEC) and Energy-to-Mass Efficiency (EEMS). Results indicated that, under equivalent DLI, the Gaussian profile increased energy costs (higher SEC) without proportional biomass gains for most spectra. The Red–Constant treatment achieved the highest efficiency ($10.02\,\mathrm{g\,kWh^{-1}}$), whereas white light exhibited the highest energy cost. Principal Component Analysis (PCA) reinforced that energy performance (SEC/EEMS) was more strongly associated with production outcomes (biomass) than with instantaneous photosynthetic metrics (e.g., F_v/F_m), underscoring the importance of continuous monitoring of energy use and yield. The PVFS proved to be a robust tool for energy benchmarking and the standardization of lighting recipes in vertical farming.

1. Introduction

Global population growth and rapid urbanization impose increasing pressure on food production, necessitating agricultural systems that are more sustainable, efficient, and resilient. In this context, vertical farms—or *plant factories with artificial lighting* (PFALs), within the broader scope of controlled-environment agriculture (CEA)—have emerged as a promising alternative. They enable the production of high-value leafy crops and microgreens in tightly controlled environments, optimizing the use of space, water, and inputs while reducing dependence on external climatic conditions [1–3].

Despite this potential, the technical and economic feasibility of indoor agriculture relies heavily on the control and efficiency of artificial lighting. Lighting often accounts for a substantial share of energy use in PFALs and is a key determinant of photosynthesis, growth, and product quality [4–8]. Beyond spectral composition, the *temporal profile* of photosynthetic photon flux density (PPFD) delivery—such as Constant versus Gaussian profiles—may alter physiological responses and, crucially, the energy–biomass relationship, even when the daily light integral (DLI) remains equivalent. Therefore, evaluating temporal profiles requires moving beyond physiological *proxies* to incorporate energy–production metrics, such as specific energy consumption (SEC; $\mathrm{kWh\,g^{-1}}$)

* Corresponding authors.
E-mail addresses: marlus.silva@ifgoiano.edu.br (M. Dias Silva), fabiano.silva@ifgoiano.edu.br (F. Guimarães Silva).

https://doi.org/10.1016/j.atech.2026.102105
Received 14 February 2026; Received in revised form 11 April 2026; Accepted 11 April 2026
Available online 7 May 2026

and energy-to-mass efficiency (EEMS; g kWh^{-1}), supported by traceable electrical monitoring.

Advances in digital technologies, IoT, and data analytics have accelerated the development of intelligent solutions for CEA, integrating sensors, actuators, and analytical platforms in near real-time [9–11,42]. Recent studies exemplify this trend by combining monitoring and computational modeling for decision support. Examples include approaches based on spectral indices and computer vision for crop monitoring in vertical farms [12,13], dynamic protocols to improve resource-use efficiency in soilless systems [14], and open platforms for control and automation [15]. Existing indoor-farming and smart-agriculture platforms already provide important capabilities such as modular sensing, remote dashboards, actuator control, automated logging, cloud-enabled analytics, and adaptive lighting control [43,49,50,52,53]. However, these systems are typically oriented toward usability, affordability, scalability, automation, or communication responsiveness, rather than toward experimentally auditable execution of lighting protocols. Smart-farming literature also highlights persistent challenges related to fragmented, inconsistent, and heterogeneous IoT data, lack of standards, and the need to ensure the accuracy of transmitted data [48,51]. In indoor cultivation, this distinction is especially relevant because DLI directly influences biomass accumulation and energy-use efficiency [47]; thus, assuming treatment equivalence from nominal setpoints alone, without validating the delivered PPFD trajectory over time, may limit reproducibility and cross-study benchmarking. Nevertheless, solutions that integrate (i) programmable temporal profiles under a target DLI, (ii) continuous electrical measurement (power/energy), (iii) an analytical *pipeline* (statistical and multivariate) oriented toward energy–biomass indicators, and (iv) telemetry-based verification of timestamp coherence, data integrity, and achieved DLI equivalence in a unified and reproducible manner remain scarce. This gap is particularly relevant given the need for benchmarking and standardization of energy metrics in vertical farms [5] and the demand for integrated instrumentation in multi-objective optimization strategies under dynamic lighting [16]. Unlike existing indoor-farming platforms that primarily emphasize monitoring, automation, or cloud analytics, the PVFS was specifically designed to make dynamic lighting protocols experimentally auditable by coupling edge-executed setpoints with time-synchronized telemetry, QA/QC metrics for sampling regularity and completeness, and telemetry-derived validation of achieved DLI equivalence.

Due to their short growth cycle and high density of bioactive compounds, microgreens have gained prominence as a crop of interest, with increasing demand and the potential to enhance the nutritional value of diets [17–19]. Sesame (*Sesamum indicum* L.), although traditionally cultivated as an oilseed crop, is also a promising candidate for microgreen production due to the functional and nutritional value of its foliage. Young sesame leaves have been reported to contain diverse iridoids and polyphenols, including acteoside, with marked antioxidant and antiglycation activity, and acteoside accumulation in leaves has reached up to 12.9% of dry weight at specific growth stages [20]. In addition, sesame leaves have been described as a nutrient-rich edible leafy vegetable, with balanced amino acid composition and high levels of minerals and vitamins, including Ca, Se, and vitamins A, C, D, and B_2, in some cases exceeding values reported for commonly consumed vegetables [46]. These attributes make sesame especially attractive for PFAL-based microgreen production, where rapid-cycle crops with high functional value are of particular interest. However, knowledge gaps persist regarding how temporal PPFD profiles and different light spectra affect the growth, photochemistry, and productivity of sesame microgreens when energy performance is jointly evaluated with physiological responses.

This study presents and experimentally validates a *Precision Vertical Farming System* (PVFS) for PFAL research, where lighting protocols shift from purely textual descriptions to executable and auditable prescriptions supported by telemetry. The PVFS combines programmable control of temporal PPFD profiles under a target DLI, continuous logging of environmental and electrical variables, and an integrated analytical workflow to relate physiological performance and production to energy costs. To ensure reproducibility and auditability, the source code and associated services are made openly available.

Accordingly, the objective of this study was to develop and validate the PVFS and apply it to sesame microgreens production using a 2×4 factorial design (Constant and Gaussian profiles × four spectra), maintaining a fixed photoperiod and equivalent DLI. Operational compliance was verified via telemetry, and the effects of profile and spectrum were assessed on growth, pigments, chlorophyll fluorescence, and energy–biomass metrics (specific energy per area, AEC; dry mass yield per area, MSA; SEC/EEMS) using ANOVA and PCA.

2. Materials and methods

The experiment was conducted under controlled conditions using a 2×4 factorial design (Constant vs. Gaussian × four spectra), with equivalent DLI and six trays per treatment ($n = 6$; 48 experimental units). The PVFS executed the lighting protocols and logged environmental and electrical telemetry to ensure traceability. Growth, biomass, pigments, and chlorophyll fluorescence were evaluated, as well as AEC, MSA, SEC, and EEMS. Effects were tested by ANOVA/Tukey ($\alpha = 0.05$) and PCA, and operational compliance was verified through telemetry validation.

2.1. Overview and relevance of the PVFS architecture

The *Precision Vertical Farming System* (PVFS) was designed as a five-layer architecture (Fig. 1) that follows a common IoT platform view of layered separation of concerns-physical assets, edge devices, infrastructure services, communication interfaces, and applications-and adapts it to PFAL experimentation to make protocol execution and data provenance verifiable via telemetry [21,22]. In the PVFS, each control action (e.g., per-channel dimming/PPFD) is recorded with a reliable timestamp and is traceably linked to environmental and energy variables measured over the same interval, enabling audit-ready reconstruction of the executed lighting trajectory and its corresponding system response.

As illustrated in Fig. 1, localizing sensing, actuation, and local control at the edge reduces command-to-record latency and improves responsiveness, which is a core motivation for edge computing in smart agriculture [23,24]. Control and telemetry exchange follow an asynchronous publish/subscribe model over MQTT, a lightweight protocol widely used in IoT deployments [25–27]. To ensure temporal coherence across control events and measurements, PVFS timestamps messages in UTC and disciplines device clocks using the Network Time Protocol (NTP), enabling consistent time-series reconstruction (e.g., PPFD trajectories and DLI integration) and automated detection of gaps or anomalies [28]. Where bidirectional streaming is required (e.g., live telemetry dashboards), WebSocket provides a standardized full-duplex transport [29].

Overall, this architecture enables the PVFS to operate not only as an instrumented growth chamber but also as an evidence-oriented experimental infrastructure: protocol reproducibility becomes testable against persisted telemetry, and agronomic outcomes can be interpreted alongside operational and energy metrics (e.g., SEC and EEMS) derived from the same auditable record.

2.2. Experimental setup and cultivation conditions

The experiment was conducted under controlled conditions in a controlled-environment agriculture facility in Brazil. In each experimental unit, 1.28 g of sesame seeds (*Sesamum indicum* L.; ~480 seeds) were sown in trays (20 cm × 14 cm × 6.5 cm) filled with 100 g of a commercial substrate moistened with 25 mL of water and kept in the dark for 12 h. The trays were then transferred to a growth chamber with four shelves (Fig. 2) and four spectral compositions: cool white 6500 K

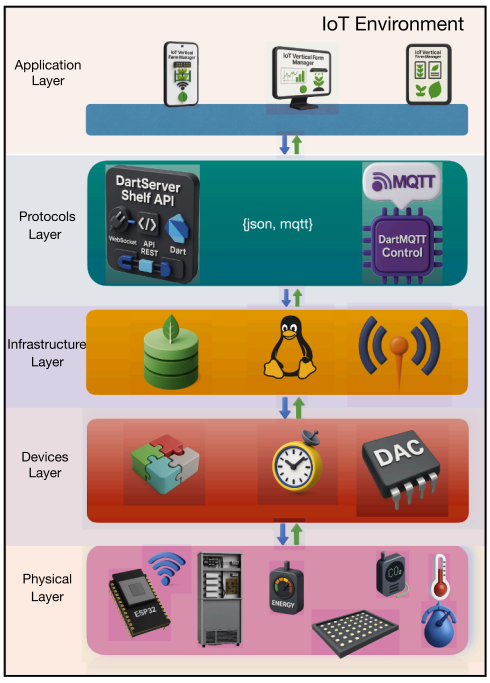

Fig. 1. PVFS five-layer architecture for PFAL experimentation. The Physical layer comprises the growth chamber, LED fixtures, environmental sensors, and electrical metering. The Devices layer executes lighting setpoints at the edge and acquires synchronized telemetry, including UTC timestamping and scheduled multi-channel dimming. The Infrastructure layer hosts messaging and persistence services (MQTT broker and a document-oriented database), storing raw telemetry and derived aggregations for querying and analysis. The Protocols layer defines standardized message interfaces for control and telemetry (e.g., JSON over MQTT) and exposes query/notification services (e.g., REST/WebSocket). The Application layer (IoT Vertical Farm Manager) supports treatment configuration, near real-time monitoring, and data export. Implementation details are provided in the Supplementary Material (Sections S1–S6).

(400–700 nm), red (peak 660 nm), blue (peak 440 nm), and RBW (70.5% red, 8.5% green, and 21.0% blue).

Microgreens were cultivated under a 12 h photoperiod (06:30–18:30) using two temporal lighting profiles: Constant (PPFD = 250 µmol m^{-2} s^{-1}) and Gaussian (PPFD = 85 µmol m^{-2} s^{-1} to 500 µmol m^{-2} s^{-1}, with automatic dimming via PVFS), while maintaining equivalent DLI (10.80 mol m^{-2} d^{-1}). PPFD and spectrum were verified using an LI-180 spectroradiometer (LI-COR, USA). Profiles were conducted in two consecutive 10-day trials.

Irrigation was adjusted to crop water demand (25 mL/d up to 7 DAS and 35 mL/d from 8 DAS onward). Environmental variables, including air temperature, relative humidity, and CO_2 concentration, were continuously logged throughout both experimental windows. Time-series stability analyses for these variables are presented in Supplementary Section S8 to document the chamber microclimate under the Constant and Gaussian windows. The 2 × 4 design (profile × spectrum) included six trays per combination ($n = 6$; 48 experimental units). At 10 DAS, chlorophyll *a* fluorescence, pigments, and biomass were evaluated; the tray was considered the experimental unit, and plant-level measurements were averaged per tray.

2.3. Growth and biomass assessment

For growth assessment, each replicate consisted of multiple seedlings. Fifteen plants were selected per replicate to measure hypocotyl length (CHL) and total leaf area (CTLA). These variables were obtained from images analyzed in ImageJ, as described by [30]. For statistical inference, plant-level measurements were aggregated as tray means (subsamples), preserving the tray as the independent experimental unit.

The remaining plants in each replicate were used to determine fresh and dry mass of hypocotyls and leaves. Samples were weighed on an analytical balance to obtain fresh mass and then dried in a forced-air circulation oven (Tecnal, TE-394/1, Brazil) at 65 °C for 48 h to determine dry mass.

Fig. 2. Representation of the controlled growth environment.

2.4. Chlorophyll a fluorescence

Chlorophyll *a* fluorescence parameters were obtained using an IMAGING-PAM fluorometer (MAXI version) and Imaging Win software (Heinz Walz GmbH, Effeltrich, Germany). Seedlings were individually fixed on a holder at 18.5 cm from a CCD camera coupled to the instrument. Fluorescence was measured on the adaxial leaf surface after 30 min of dark adaptation to ensure full opening of reaction centers. Under this condition, tissues were exposed to a low-intensity measuring light (0.03 µmol m^{-2} s^{-1}) to determine initial fluorescence (Fo). Next, a saturating light pulse (> 6000 µmol m^{-2} s^{-1}) was applied for 0.8 s to determine maximal fluorescence (Fm), and the maximum quantum yield of PSII was computed (Fv/Fm = (Fm – Fo) / Fm) [31].

After illuminating the sample for 40 s, fluorescence under light-adapted conditions was recorded to obtain actinic-light variables such as the effective quantum yield of PSII, Y(II), and non-photochemical quenching (NPQ) [32]. The photochemical quenching coefficient was calculated using standard PAM definitions, $q_P = (F'_m - F_s)/(F'_m - F'_0)$, as implemented in ImagingWin. Electron transport rate (ETR) was calculated as ETR = Y(II) × PAR × A_{leaf} × 0.5 [33], where PAR is photosynthetically active radiation (photon flux density), A_{leaf} is the fraction of incident light absorbed by leaves, and 0.5 is the fraction of excitation energy assumed to be equally distributed between PSII and PSI [34]. When not directly measured, A_{leaf} and actinic irradiance followed the equipment/software settings used in ImagingWin.

2.5. Photosynthetic pigments

Pigment concentrations were determined after extraction with dimethyl sulfoxide (DMSO) saturated with calcium carbonate ($CaCO_3$) [35]. Chlorophyll *a* (Chl*a*), chlorophyll *b* (Chl*b*), and carotenoids (Cart) were quantified using a UV–vis spectrophotometer (Evolution 60S, Thermo Fisher Scientific Inc., MA, USA) at 665, 649, and 480 nm, respectively. Calculations followed the equations proposed by [36], and results were expressed as $\mu g\ g^{-1}$ of leaf fresh mass.

2.6. Calculation of specific energy consumption (SEC) and energy mass efficiency (EEMS)

Specific energy consumption (SEC) was calculated from areal energy consumption (AEC, kWh m^{-2}) and dry mass yield per area (MSA, g m^{-2}).

Areal energy consumption was defined as:

$$\mathrm{AEC} = \frac{E_{\mathrm{tot}}}{A}, \tag{1}$$

where E_{tot} is the total electrical energy consumed during cultivation (kWh) and A is the illuminated area (m^2). When only mean power P (W) and time t (h) were available, we used:

$$E_{\mathrm{tot}} = \frac{P \cdot t}{1000}. \tag{2}$$

Dry mass yield per area was estimated as:

$$\mathrm{MSA} = M_{\mathrm{sec}} \cdot N_m, \tag{3}$$

where M_{sec} is the mean dry mass per seedling (g) and N_m is seedling density (seedlings m^{-2}).

Specific energy consumption was then computed as:

$$\mathrm{SEC} = \frac{\mathrm{AEC}}{\mathrm{MSA}} \quad \left(\mathrm{kWh\,g^{-1}}\right). \tag{4}$$

From this relationship, energy mass efficiency (EEMS) was defined as the inverse of SEC, expressing the amount of dry biomass obtained per unit of consumed energy:

$$\mathrm{EEMS} = \frac{1}{\mathrm{SEC}} \quad \left(\mathrm{g\,kWh^{-1}}\right). \tag{5}$$

Thus, SEC and EEMS are complementary metrics: SEC indicates the energy cost per gram of dry mass produced, whereas EEMS represents biomass return per unit of electrical energy used.

For N_m, 480 seeds per tray (0.028 m^2) were considered, equivalent to 17 142 seeds m^{-2}, adjusted by the observed germination rate of 85%, resulting in 14 571 seedlings m^{-2}. The adopted thermal conditions (20–30 °C) agree with reports for *Sesamum indicum*, indicating high germination rates within this range, supporting the 85% adjustment [37–39].

2.7. Statistical analysis

All data processing and statistical analyses were performed in Python (v3.9.6) using widely adopted scientific libraries, including *pandas* for data handling, *statsmodels* for ANOVA and post-hoc comparisons, and *scikit-learn* for multivariate analysis. A fully reproducible workflow (code and datasets) will be made publicly available upon acceptance.

Data were first inspected by exploratory analysis. To mitigate the influence of outliers without excluding observations, extreme values were winsorized within each treatment cell (*Profile* × *Light*) using Tukey's IQR fences: values below $Q_1 - 1.5 \times IQR$ were set to the lower fence and values above $Q_3 + 1.5 \times IQR$ were set to the upper fence. Winsorization was applied only when $IQR > 0$ and the cell contained at least four non-missing observations.

For each response variable, a two-way factorial ANOVA was fitted with fixed effects of *Profile*, *Light*, and their interaction ($\alpha = 0.05$). Model assumptions were evaluated by residual diagnostics, including normality (Shapiro–Wilk test) and visual inspection of residuals versus fitted values and scale–location plots. When significant effects were detected, means were separated using Tukey's HSD as implemented in *statsmodels*. When the interaction term was significant, simple effects were evaluated (*Profile* within each *Light* and *Light* within each *Profile*).

Multiple comparisons were summarized using a compact letter display (CLD): uppercase letters compare *Profiles* within each *Light*, whereas lowercase letters compare *Lights* within each *Profile*. Results are reported as mean ± standard error (SE).

Multivariate patterns were assessed by principal component analysis (PCA) on tray-level observations ($n = 48$) after centering and unit-variance scaling (autoscaling). Pearson correlation coefficients were also computed. PCA scores, variable loadings, and the proportion of variance explained by each component are reported.

2.8. Telemetry validation and PVFS operational compliance

Operational compliance of the *Precision Vertical Farming System* (PVFS) was verified in both experimental windows (Constant: 08–18 March 2024; Gaussian: 22 March–01 April 2024) through (i) time-series quality control, (ii) DLI calculation from PPFD telemetry, and (iii) Gaussian-profile validation via model fitting.

2.8.1. Acquisition and preprocessing

Telemetry (per-channel PPFD and environmental variables) was collected via MQTT and persisted in MongoDB. Records were stored with UTC timestamps (ISO-8601) and converted to the local time zone (`America/Sao_Paulo`) only for photoperiod segmentation. For summary metrics and comparative plots, series were resampled to a fixed 10 s step using mean aggregation. In addition to the PPFD-focused validation reported below, environmental time series for air temperature, relative humidity, and CO_2 concentration were examined to document chamber microclimate stability across the Constant and Gaussian windows; these complementary analyses are summarized in Supplementary Section S8.

2.8.2. Time-series QA/QC (integrity, jitter, and gaps)

Quality Assurance (QA) and Quality Control (QC) procedures were applied to verify telemetry integrity and sampling-interval regularity. Evaluation was conducted on raw series (without resampling) using forward differences $\Delta t_i = t_{i+1} - t_i$. For each topic, the median interval, the IQR of Δt (sampling-interval variability; *jitter*), and the largest gap were reported; gaps were defined when $\Delta t_i > 60$ s. Completeness was estimated as the ratio between the number of observed samples and the expected number, given the observed duration and nominal interval. Metrics were also computed *per day* within the light window (06:30–18:30, local time), to report daily completeness and identify days with partial data loss.

2.8.3. Telemetry-derived DLI

Daily light integral (DLI; mol m^{-2} d^{-1}) was calculated by integrating instantaneous PPFD (μmol m^{-2} s^{-1}) over the photoperiod:

$$\mathrm{DLI} = \frac{1}{10^6} \sum_i \mathrm{PPFD}_i \cdot \Delta t_i, \tag{6}$$

where Δt_i is the time step (s) and the summation spans the light window. To reduce bias due to missing data, Δt_i was capped at 120 s during integration, and integration was clipped to the photoperiod end to avoid night-gap inflation (see Supplementary S7 for the sensitivity analysis and formulation). Equivalence of daily DLI relative to the nominal target was assessed using TOST, with equivalence bounds of ±5% of the target and $\alpha = 0.05$ (90% CI) [40].

2.8.4. Inter-channel uniformity

Inter-channel uniformity (ch1–ch4) was quantified by: (i) instantaneous CV% across channels at each resampled point during the photoperiod; and (ii) daily CV% across channels for daily DLI.

2.8.5. Gaussian-profile validation via model fitting

Under the Gaussian profile, temporal compliance was assessed by fitting a Gaussian function to the measured PPFD series for each channel, per day, within the photoperiod. Local time was normalized to $x \in [0, 1]$ and the following model was fitted:

$$\hat{y}(x) = c_0 + c_1 \exp\left(-\frac{1}{2}\left(\frac{x-\mu}{\sigma}\right)^2\right). \quad (7)$$

For fitting, PPFD was resampled to 30 s (mean). On a predefined grid of (μ, σ), c_0 and c_1 were estimated by linear least squares, and the best fit was selected by the lowest RMSE (*root mean square error*). Fit quality was summarized by RMSE, MAE (*mean absolute error*), and R^2, defined as:

$$\mathrm{RMSE} = \sqrt{\frac{1}{n}\sum_{i=1}^{n}(y_i - \hat{y}_i)^2}, \qquad \mathrm{MAE} = \frac{1}{n}\sum_{i=1}^{n}|y_i - \hat{y}_i|, \quad (8)$$

where y_i and $\hat{y}_i$ are the observed and fitted PPFD values, respectively. Peak time was derived from μ and the photoperiod limits; the procedure was repeated daily to identify days with operational deviations.

3. Results

Three sets of variables were evaluated: (i) photosynthetic pigments—chlorophyll *a* (*Chla*), chlorophyll *b* (*Chlb*), carotenoids (*Cart*), and the *Chla* : *Chlb* ratio; (ii) growth and morphology—hypocotyl length (*CHL*), total leaf area (*CTLA*), hypocotyl fresh weight (*HFW*), leaf fresh weight (*LFW*), leaf dry mass (*LMD*), total dry mass (*TMD*), and hypocotyl dry mass (*HMD*); and (iii) PSII photochemical parameters and energy-performance metrics—effective quantum yield $Y(\mathrm{II})$, maximum quantum efficiency F_v/F_m, non-photochemical quenching (NPQ), photochemical quenching coefficient (q_P), electron transport rate (ETR), specific energy consumption (SEC, $\mathrm{kWh\,g^{-1}}$), and its inverse, Energy-to-Mass Efficiency (EEMS, $\mathrm{g\,kWh^{-1}}$). Analyses considered the effects of lighting profiles (Constant and Gaussian), light spectra (blue, RBW, red, and white), and their interaction. Unless otherwise stated, values represent tray means (experimental unit; $n = 6$ per treatment), with plant-level measurements treated as subsamples aggregated by tray.

Photosynthetic pigment concentrations (Fig. 3) showed a significant *profile* × *light spectrum* interaction. Higher chlorophyll *a* (*Chla*) values (Fig. 3a) were observed under white, RBW, and blue light in the Constant profile. In contrast, under red light, the pattern was reversed, with *Chla* higher in the Gaussian than in the Constant profile. Within each profile, there were no differences among white, RBW, and blue, but all differed from red. In the Constant profile, red light resulted in significantly lower *Chla* than the other treatments, whereas in the Gaussian profile, red light produced the highest *Chla* compared with the other light spectra.

For chlorophyll *b* (*Chlb*) (Fig. 3b), the highest values occurred under white and red light in the Gaussian profile, whereas under RBW the highest values occurred in the Constant profile. Under blue light, no significant differences between profiles were detected.

Carotenoids (*Cart*) (Fig. 3c) differed between profiles under white, RBW, and red light, always with higher values in the Gaussian profile. Under blue light, no significant differences were observed.

The *Chla* : *Chlb* ratio (Fig. 3d) was higher in the Constant profile under white, RBW, and red light, whereas under blue light there was no significant difference between profiles.

Under white and red light, *Chlb* showed higher values in the Gaussian profile, whereas *Cart* also showed higher values in the Gaussian profile under white and red light (Fig. 3).

Electron transport rate (ETR) (Fig. 4d) differed significantly only under white light, with higher values in the Constant profile compared with the Gaussian profile.

The F_v/F_m ratio (Fig. 4a) differed between profiles under RBW and blue light, with higher values in the Gaussian profile. Under white and red light, there were no significant differences between profiles. Within the Constant profile, white and blue did not differ from each other, but both were higher than RBW, and red was lower than all other light spectra.

Non-photochemical quenching (NPQ) (Fig. 4e) differed only under white light, with higher values in the Gaussian profile. In the Constant profile, NPQ was higher under blue and red light than under white and RBW.

The effective quantum yield of PSII, $Y(\mathrm{II})$, and the photochemical quenching coefficient, q_P (Fig. 4(b) and (c), also differed under white light, with higher values in the Constant profile. Lower $Y(\mathrm{II})$ and q_P values were observed under blue and red light in the Constant profile, whereas in the Gaussian profile q_P was reduced under blue light.

Specific energy consumption (SEC; $\mathrm{kWh\,g^{-1}}$) (Fig. 4f) differed between profiles under RBW, blue, and red light, with higher values in the Gaussian profile. Under white light, there were no significant differences between profiles. Within the Constant profile, white light showed higher SEC than RBW, blue, and red, which did not differ from each other. Within the Gaussian profile, white light showed higher SEC than blue light, and blue light was higher than RBW and red, which did not differ from each other.

Hypocotyl length (CHL) (Fig. 5a) differed between profiles only under blue light, with higher values in the Constant profile than in the Gaussian profile. Within the Constant profile, white, blue, and red did not differ from each other and all were higher than RBW. In the Gaussian profile, white and red (not differing from each other) were higher than RBW and blue, which in turn did not differ from each other.

Total leaf area (CTLA) (Fig. 5b) showed no significant differences between profiles; within each profile, comparisons among light spectra were limited.

Hypocotyl fresh weight (HFW) (Fig. 5c) was higher in the Constant profile for all light spectra except RBW, for which there was no difference between profiles. Within the Constant profile, red showed the highest HFW, whereas white and RBW showed the lowest values. In the Gaussian profile, RBW showed lower HFW than the other light spectra.

Leaf fresh weight (LFW) (Fig. 5d) differed under white light, with higher values in the Gaussian profile. Under RBW, blue, and red light, there were no significant differences between profiles. Within the Constant profile, LFW under white light was lower than under the other light spectra.

Leaf dry mass (LMD) (Fig. 5e) differed under blue and red light, with higher values in the Constant profile. Under white and RBW light, there were no significant differences between profiles. Within the Constant profile, LMD was lower under white light than under the other light spectra.

Total dry mass (TMD) (Fig. 5f) differed under RBW, blue, and red light, always with higher values in the Constant profile. Under white light, there was no significant difference. Within the Constant profile, TMD was lower under white and RBW than under blue and red.

Hypocotyl dry mass (HMD) (Figure 5g) was higher in the Constant profile under RBW, blue, and red light. Under white light, there was no significant difference between profiles. The highest HMD values occurred under red light compared with the other light spectra.

In the Constant profile (Table 1), the red spectrum showed the lowest SEC ($0.0998\ \mathrm{kWh\,g^{-1}}$) and the highest EEMS ($10.02\ \mathrm{g\,kWh^{-1}}$). In the same profile, white light showed the highest SEC ($0.2341\ \mathrm{kWh\,g^{-1}}$) and the lowest EEMS ($4.27\ \mathrm{g\,kWh^{-1}}$).

In the Gaussian profile, SEC ranged from $0.1585\ \mathrm{kW\,h\,g^{-1}}$ to $0.2744\ \mathrm{kW\,h\,g^{-1}}$, whereas EEMS ranged from $3.64\ \mathrm{g\,kW^{-1}\,h}$ to $6.31\ \mathrm{g\,kW^{-1}\,h}$ (Table 1). Red light showed the lowest SEC ($0.1585\ \mathrm{kW\,h\,g^{-1}}$) and the highest EEMS ($6.31\ \mathrm{g\,kW^{-1}\,h}$), whereas white light showed the highest SEC ($0.2744\ \mathrm{kW\,h\,g^{-1}}$) and the lowest EEMS ($3.64\ \mathrm{g\,kW^{-1}\,h}$).

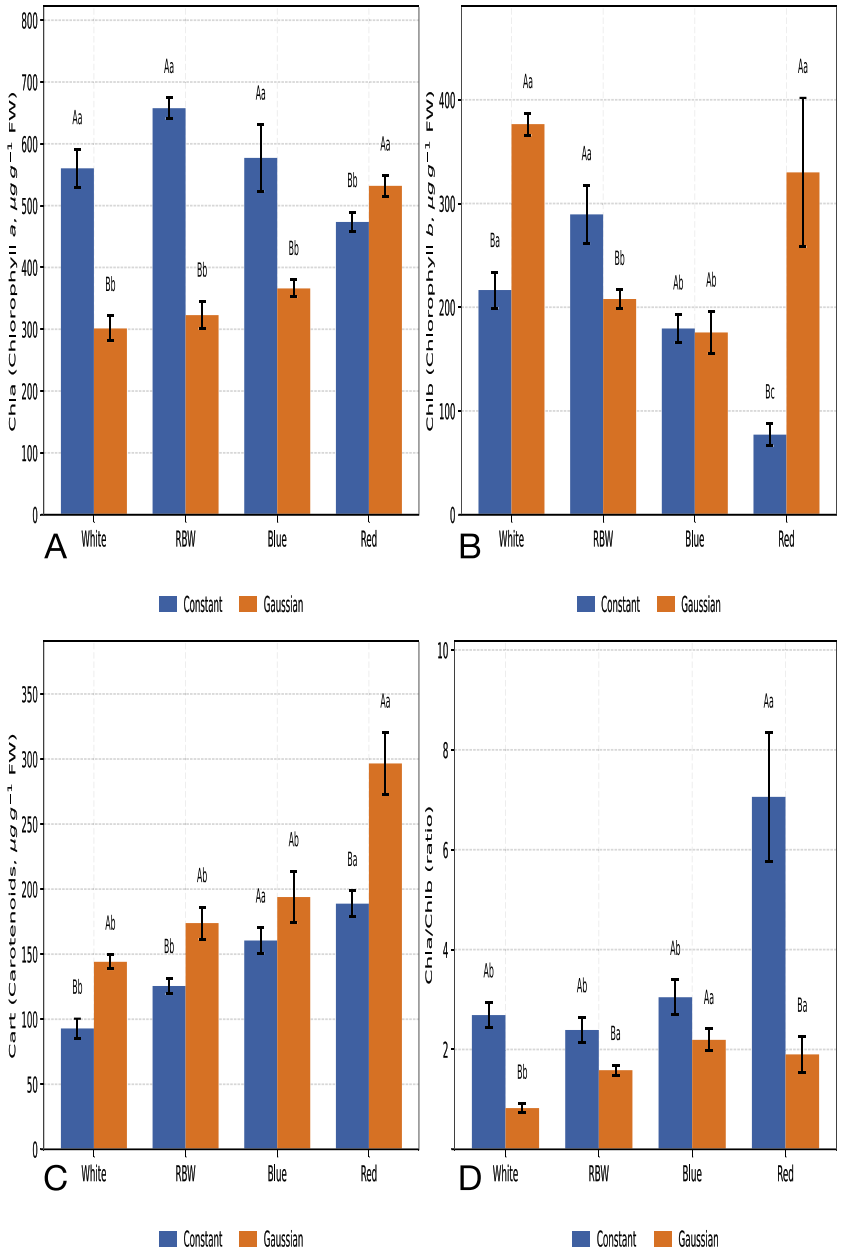

Fig. 3. Photosynthetic pigments and the *Chla* : *Chlb* ratio under two lighting profiles (Constant and Gaussian) and four light spectra (blue, RBW, red, and white; RBW = red–blue–white combination). Panels: (A) *Chla*; (B) *Chlb*; (C) *Cart*; (D) *Chla* : *Chlb*. Units: $\mu g\, g^{-1}$ fresh mass (A–C); dimensionless (D). Bars = mean ± SE. Uppercase letters compare *Profiles* within each *Light*; lowercase letters compare *Lights* within each *Profile*. (For interpretation of the references to colour in this figure legend, the reader is referred to the web version of this article.)

Table 1
Areal energy consumption (AEC), dry mass yield per area (MSA), specific energy consumption (SEC), and Energy-to-Mass Efficiency (EEMS) under different light spectra and lighting profiles. Seedling density was corrected based on the observed germination rate of 85%. SEC was calculated from full-precision AEC and MSA values prior to rounding.

	Constant				Gaussian			
Spectrum	AEC ($kWh\, m^{-2}$)	MSA ($g\, m^{-2}$)	SEC ($kWh\, g^{-1}$)	EEMS ($g\, kWh^{-1}$)	AEC ($kWh\, m^{-2}$)	MSA ($g\, m^{-2}$)	SEC ($kWh\, g^{-1}$)	EEMS ($g\, kWh^{-1}$)
Blue	13.51	104.33	0.1309	7.64	17.81	80.47	0.2232	4.48
RBW	12.24	96.09	0.1282	7.80	14.47	81.03	0.1793	5.58
Red	12.11	123.37	0.0998	10.02	13.25	83.95	0.1585	6.31
White	16.37	71.80	0.2341	4.27	23.09	84.43	0.2744	3.64

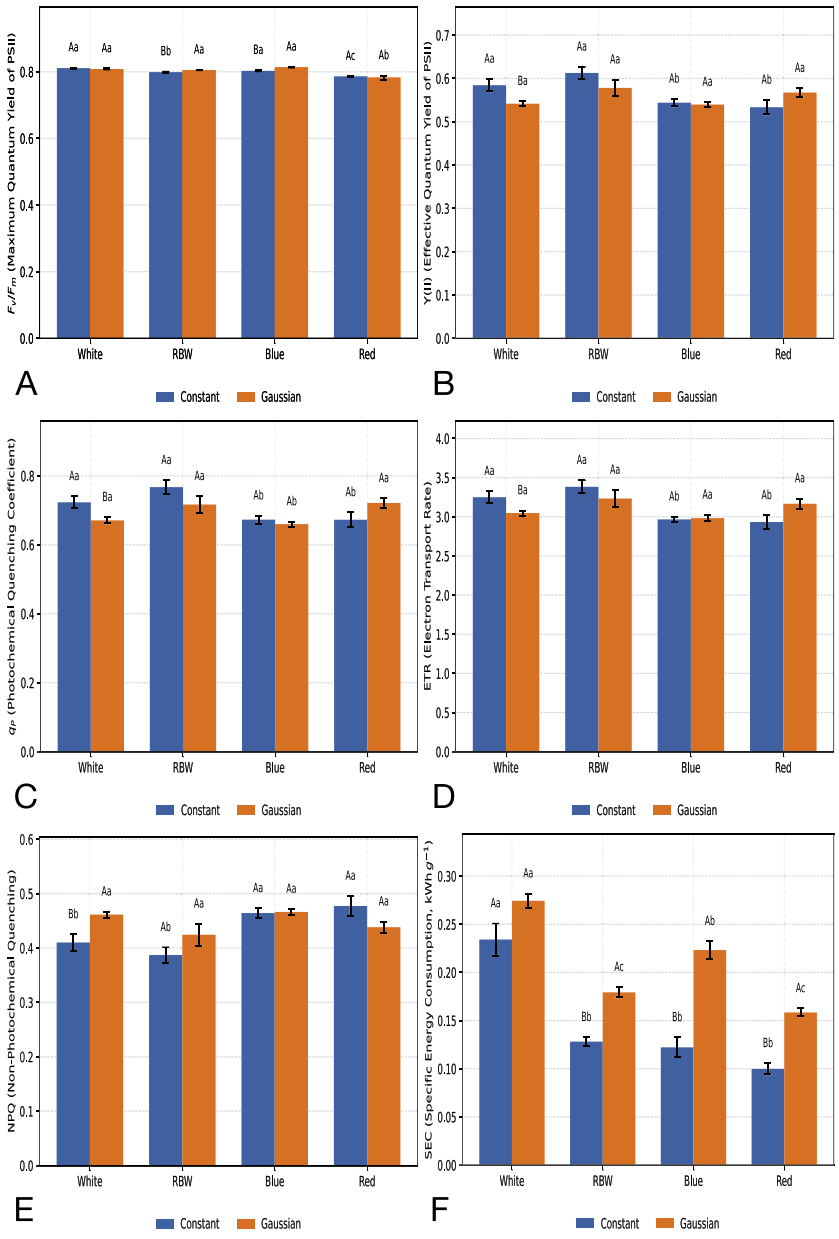

Fig. 4. PSII photochemical parameters and specific energy consumption (SEC) under Constant and Gaussian profiles across four light spectra (blue, RBW, red, and white). Panels: (A) F_v/F_m (maximum quantum yield of PSII); (B) $Y(II)$ (effective quantum yield of PSII); (C) q_P (photochemical quenching coefficient); (D) ETR (electron transport rate); (E) NPQ (non-photochemical quenching); (F) SEC, representing energy cost per unit biomass. Uppercase letters indicate differences between profiles within the same light, and lowercase letters indicate differences among lights within the same profile (Tukey, $\alpha = 0.05$). (For interpretation of the references to colour in this figure legend, the reader is referred to the web version of this article.)

Between profiles, differences in SEC were observed under RBW, blue, and red light, whereas under white light no significant difference between profiles was detected (Fig. 4f).

3.1. Multivariate analysis (PCA)

Principal Component Analysis (PCA) summarized the multivariate structure of morphological, physiological, pigment, and energy-performance variables. The first four components explained 76.47% of the total variance (PC1 = 34.37%, PC2 = 22.46%, PC3 = 11.30%, PC4 = 8.35%; Table 2).

PC1 showed strong correlations with NPQ ($r = -0.81$) and biomass traits (HFW: $r = -0.76$; HMD: $r = -0.77$; TMD: $r = -0.79$), and positive correlations with photochemical variables, including $Y(II)$ ($r = 0.78$), q_P ($r = 0.74$), and ETR ($r = 0.82$). SEC showed a moderate correlation with PC1 ($r = 0.53$) and a strong correlation with PC2 ($r = -0.76$).

PC2 showed positive correlations with *Chla* ($r = 0.67$), q_P ($r = 0.63$), $Y(II)$ ($r = 0.56$), and the *Chla* : *Chlb* ratio ($r = 0.54$), and a negative correlation with SEC ($r = -0.76$). PC3 was associated with leaf mass variables (LFW: $r = 0.84$; LMD: $r = 0.71$). PC4 showed correlation with F_v/F_m ($r = -0.70$) and *Chlb* ($r = 0.63$).

In the biplot (Fig. 6), vectors for $Y(II)$, q_P, and ETR showed similar directions, whereas NPQ pointed in the opposite direction. Biomass variables projected on the negative side of PC1, and SEC projected in the opposite direction to biomass variables. Treatments showed partial overlap in the scores on the first two components.

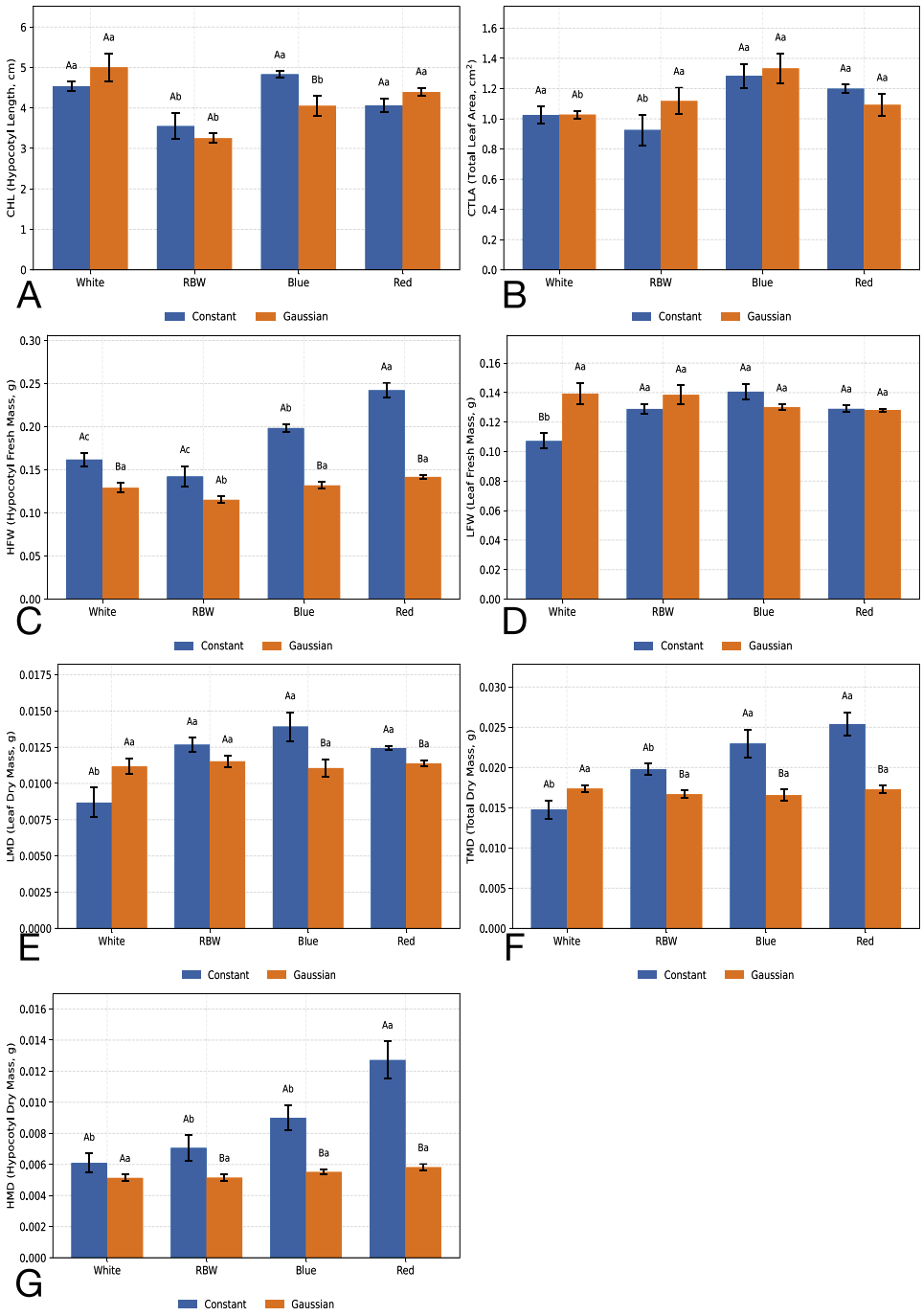

Fig. 5. Growth and morphology under Constant and Gaussian profiles across four light spectra (blue, RBW, red, and white). Panels: (A) CHL; (B) CTLA; (C) HFW; (D) LFW; (E) LMD; (F) TMD; (G) HMD. Bars = mean ± SE. Letters indicate differences by Tukey's test ($\alpha = 0.05$), with uppercase letters comparing *Profiles* and lowercase letters comparing *Light spectra*. (For interpretation of the references to colour in this figure legend, the reader is referred to the web version of this article.)

3.2. Correlation analysis

The Pearson correlation matrix (r) is shown in Fig. 7. All pairwise correlations are displayed (no significance filtering). Associations were classified as strong ($|r| \geq 0.70$), moderate ($0.30 \leq |r| < 0.70$), and weak ($|r| < 0.30$).

$Y(II)$ was strongly and positively correlated with q_P ($r = 0.98$) and ETR ($r = 0.97$), and strongly and negatively correlated with NPQ ($r = -0.99$). q_P and ETR were strongly and positively correlated ($r = 0.95$), and both were strongly and negatively correlated with NPQ ($r = -0.97$ for q_P vs. NPQ and $r = -0.97$ for ETR vs. NPQ). *Chla* showed a moderate correlation with q_P ($r = 0.43$) and a moderate negative correlation with NPQ ($r = -0.37$).

HFW and HMD were strongly correlated ($r = 0.86$). TMD was strongly correlated with HMD ($r = 0.88$), LMD ($r = 0.73$), and HFW ($r = 0.74$). LFW was strongly correlated with LMD ($r = 0.74$).

SEC showed a strong negative correlation with TMD ($r = -0.78$) and moderate negative correlations with HMD ($r = -0.69$), LMD ($r = -0.65$), and HFW ($r = -0.60$). Correlations of SEC with NPQ ($r = -0.04$), q_P ($r = -0.09$), and ETR ($r = 0.06$) were weak.

The *Chla* : *Chlb* ratio was moderately and negatively correlated with *Chlb* ($r = -0.68$) and weakly and positively correlated with *Chla*

Table 2
Correlation coefficients (r) between traits and the first four principal components (PC1–PC4). Values in **bold** indicate strong correlation ($|r| \geq 0.70$).

Variable (full name)	PC1	PC2	PC3	PC4
HFW (*Hypocotyl fresh weight, g*)	**−0.76**	0.39	−0.35	0.09
LFW (*Leaf fresh weight, g*)	−0.34	−0.08	**0.84**	−0.18
HMD (*Hypocotyl dry mass, g*)	**−0.77**	0.45	−0.16	−0.01
LMD (*Leaf dry mass, g*)	−0.50	0.34	**0.71**	−0.13
F_v/F_m (*Maximum quantum yield of PSII*)	0.23	−0.50	−0.06	**−0.70**
$Y(II)$ (*Effective quantum yield of PSII*)	**0.78**	0.56	0.09	−0.11
NPQ (*Non-photochemical quenching*)	**−0.81**	−0.51	−0.05	0.12
q_P (*Photochemical quenching coefficient*)	**0.74**	0.63	0.09	0.04
ETR (*Electron transport rate*)	**0.82**	0.48	0.14	−0.08
Chla (*Chlorophyll a*; µg g^{-1} FM)	0.08	0.67	−0.23	0.28
Chlb (*Chlorophyll b*; µg g^{-1} FM)	0.47	−0.30	0.32	0.63
Cart (*Carotenoids*; µg g^{-1} FM)	−0.24	0.01	0.26	0.38
TMD (*Total dry mass, g*)	**−0.79**	0.45	0.23	−0.06
SEC (*Specific energy consumption*; kWh g^{-1})	0.53	**−0.76**	−0.20	−0.04
CTLA (*Total leaf area, cm^2*)	−0.53	−0.29	0.06	−0.17
CHL (*Hypocotyl length, cm*)	−0.28	−0.45	−0.10	0.40
Chla_Chlb (*Chla* : *Chlb* ratio)	−0.48	0.54	−0.43	−0.18
Eigenvalue	5.842	3.818	1.920	1.420
Variance (%)	34.37	22.46	11.30	8.35
Cumulative (%)	34.37	56.83	68.12	76.47

($r = 0.29$). The ratio showed moderate correlations with HFW ($r = 0.64$) and HMD ($r = 0.57$), and a moderate negative correlation with SEC ($r = -0.49$). Correlations involving *Cart* were mostly weak.

3.3. Telemetry validation and PVFS operational compliance

PVFS telemetry showed high temporal regularity and high data availability across both experimental windows (Constant: 08–18/03/2024; Gaussian: 22/03–01/04/2024). Across PPFD channels ch1–ch4, the median sampling interval was 10.0 s under both profiles, with near-zero jitter (IQR of sampling intervals = 0.000–0.002 s for both profiles). The proportion of inter-sample intervals at the expected 10 s step was 99.92–99.95% (Constant) and 99.94% (Gaussian), and overall completeness was 99.80–99.86% under the Constant profile and 98.82% under the Gaussian profile (Table 3). In telemetry terms, these windows comprise 11 *photoperiod days* (inclusive dates: 08–18/03/2024 and 22/03/2024–01/04/2024), while agronomic time is reported as DAS (Day 0 = sowing on 08/03/2024 and 22/03/2024), and the crop timeline is described up to 10 DAS (i.e., through 18/03/2024 and 01/04/2024, respectively). Complementary environmental telemetry indicated that air temperature remained close to the nominal setpoint in both windows, whereas relative humidity showed a more pronounced midday depression under the Gaussian profile; these time-series stability analyses are provided in Supplementary Section S8.

In the daily assessment restricted to the photoperiod (06:30–18:30, local time), the lowest availability under the Constant profile occurred on 2024-03-12, ranging from 98.70–98.94% across channels. On that day, the largest within-photoperiod inter-sample interval reached 190–200 s, corresponding to outage gaps above 60 s (Table 3). Under the Gaussian profile, the lowest photoperiod availability was observed on 2024-03-30 (85.65%). Notably, the reduced availability on this day occurred as dispersed sample losses, because the largest inter-sample interval remained 20 s and no outage gaps above 60 s were observed on that date (Table 3). Across the Gaussian window, occasional within-photoperiod outage gaps ($\Delta t > 60$ s) were observed on a few days, with a maximum gap of approximately 137 s (e.g., 2024-04-01).

Daily DLI was estimated by integrating PPFD during the photoperiod. Mean DLI values were 10.33–10.42 mol m^{-2} d^{-1} under the Constant profile and 10.75–10.77 mol m^{-2} d^{-1} under the Gaussian profile (Table 3). The lowest daily DLI values were observed on 2024-03-08 (Constant: 10.05–10.14 mol m^{-2} d^{-1}) and 2024-03-30 (Gaussian: 10.14–10.15 mol m^{-2} d^{-1}) (Table 3). Equivalence of daily DLI relative to the target was assessed by TOST with a ±5% margin and a 90% CI criterion; equivalence was supported for all channels under both profiles when considering the distribution of daily DLI across the window (Table 3), despite these isolated low-DLI days falling slightly below the lower equivalence bound.

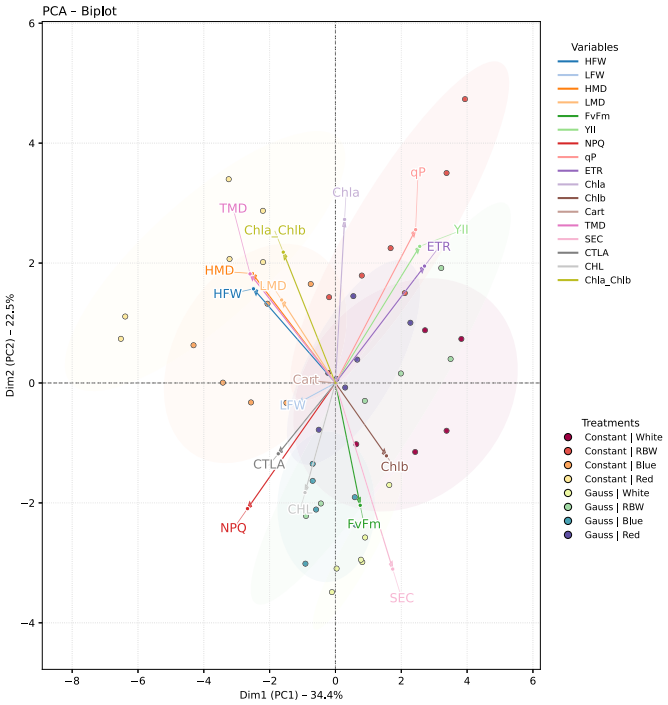

Fig. 6. PCA biplot considering morphological, photosynthetic, pigment, and energy-cost variables under different combinations of lighting profiles (Constant and Gaussian) and light spectra (blue, RBW, red, and white). Arrows represent trait vectors, with direction and length proportional to correlations with the components. Treatments are shown as points, with 90% confidence ellipses for each group. PC1 (34.37%) contrasts biomass traits and NPQ (negative scores) with photochemical performance ($Y(II)$, q_P, and ETR; positive scores). PC2 (22.46%) is mainly driven by a negative association with SEC and a positive association with *Chla* and photochemical-use indicators. (For interpretation of the references to colour in this figure legend, the reader is referred to the web version of this article.)

Daily inter-channel uniformity, quantified by the CV% of DLI across channels, was 0.37% under the Constant profile and 0.08% under the Gaussian profile (Table 3). Under the Gaussian profile, model fitting from telemetry yielded $\mu \approx 0.500$ and $\sigma \approx 0.150$–0.152, with $R^2 \approx 0.9997$–0.9998 and RMSE ≈ 1.84–2.25 across the four channels (Table 3).

4. Discussion

This study integrates two primary contributions: (i) the validation of a Precision Vertical Farming System (PVFS) capable of executing temporal lighting profiles under a target DLI, logging environmental/electrical telemetry in near real-time, and structuring data for ANOVA/Tukey and multivariate analysis; and (ii) evidence that, in sesame microgreens, the temporal shape of PPFD delivery (Constant vs. Gaussian) is associated with differences in the energy–biomass relationship, even when the daily DLI is maintained close to, and statistically equivalent to, the target across profiles.

From an engineering standpoint, the PVFS integrates control, traceability, and an analytical *pipeline* within an auditable and extensible architecture, aligning with recent advances in controlled-environment cultivation platforms and dynamic protocols [12–14]. The distinctive contribution here is coupling (a) programmable temporal profiles with setpoint-to-execution traceability, (b) continuous electrical metrology,

Table 3
Summary of key indicators for telemetry validation and PVFS operational compliance, based on PPFD channels ch1–ch4. Values reported as ranges reflect variation across channels.

Indicator	Constant (08–18/03/2024)	Gaussian (22/03–01/04/2024)
Validated PPFD channels	ch1–ch4	ch1–ch4
Sampling interval (median, s)	10.0	10.0
Jitter (IQR of sampling intervals, s)	0.000–0.002	0.000–0.002
Samples at expected step (%)	99.92–99.95	99.94
Overall completeness (% of expected samples)	99.80–99.86	98.82
Worst day within photoperiod (local)	2024-03-12	2024-03-30
Photoperiod availability on worst day (%)	98.70–98.94	85.65
Largest inter-sample interval on worst day (s)	190–200	20
Largest outage gap on worst day ($\Delta t > 60$ s) (s)	190–200	—[a]
Mean DLI (mol m^{-2} d^{-1})	10.33–10.42	10.75–10.77
DLI on worst-availability day (mol m^{-2} d^{-1})	10.34–10.43 (2024-03-12)	10.14–10.15 (2024-03-30)
Lowest daily DLI observed (mol m^{-2} d^{-1})	10.05–10.14 (2024-03-08)[d]	10.14–10.15 (2024-03-30)
DLI equivalence vs target (TOST, $\Delta = \pm 5\%$)	Equivalent (all ch, 90% CI)[b]	Equivalent (all ch, 90% CI)[b]
Daily inter-channel uniformity (CV% of DLI)	0.37	0.08
Gaussian fit : μ	—	0.500 (peak ≈ 12:30, local)[c]
Gaussian fit : σ	—	0.150–0.152
Fit quality: R^2	—	0.9997–0.9998
Fit quality: RMSE (PPFD)	—	1.84–2.25

[a] On 2024-03-30 (Gaussian profile), reduced photoperiod availability occurred as dispersed sample losses (max inter-sample interval = 20 s), without outage gaps above 60 s.

[b] TOST applied to daily DLI values with equivalence defined as $\Delta = 0.54$ mol m^{-2} d^{-1} (i.e., ±5% around 10.8 mol m^{-2} d^{-1}), using a 90% CI criterion.

[c] μ is reported on a normalized time scale over the 06:30–18:30 photoperiod (local); the peak time is estimated as 06:30 + $\mu \times 12$ h.

[d] On 2024-03-08 (Constant profile), daily DLI was slightly below the lower ±5% equivalence bound (10.26 mol m^{-2} d^{-1}), indicating an isolated low-DLI day within the Constant window.

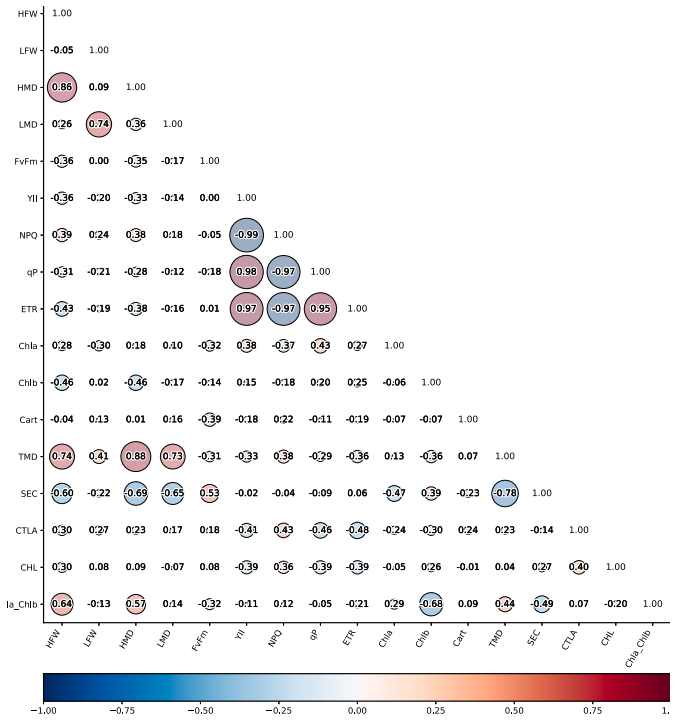

Fig. 7. Pearson correlation matrix (r) among physiological, morphological, pigment, and energy-performance variables under different combinations of lighting profiles (Constant and Gaussian) and light spectra (blue, RBW, red, and white). Red circles indicate positive correlations and blue circles indicate negative correlations, with size proportional to $|r|$. SEC represents specific energy consumption (energy cost per unit biomass). (For interpretation of the references to colour in this figure legend, the reader is referred to the web version of this article.)

and (c) actionable efficiency metrics (SEC/EEMS), providing a practical basis for multi-objective optimization and future extensions (e.g., telemetry-updated digital models) [41].

Telemetry underpins the operational comparability between profiles by documenting high temporal regularity (10 s median; IQR ≈ 0 s) and high data availability across four channels (ch1–ch4) in both experimental windows (Constant: 08–18/03/2024; Gaussian: 22/03–01/04/2024), with high overall completeness (Table 3). Restricting assessment to the photoperiod enabled the identification of days with lower availability (12/03/2024 in Constant; 30/03/2024 in Gaussian) and the quantification of gaps, making deviations explicit and auditable (Table 3). The DLI derived directly from telemetry was equivalent to the target (TOST; $\Delta = \pm 5\%$; 90% CI) and showed high inter-channel uniformity (low CV%), while in the Gaussian profile, the temporal shape was well described by a Gaussian model (high R^2 and low RMSE; Table 3). This reduces the likelihood that differences in SEC/EEMS are driven by unverified discrepancies in the daily light dose.

Complementary analyses of environmental telemetry showed that air temperature remained close to the nominal setpoint in both windows, supporting the thermal stability of the chamber during the experiment. Relative humidity exhibited greater intradiurnal variation than temperature and showed a more pronounced midday depression under the Gaussian window, consistent with stronger transient evaporative demand under dynamic PPFD. Thus, although the experiment was conducted under a stable thermal regime, the temporal shape of light delivery may also have modulated the chamber microenvironment through humidity-related responses. CO_2 was also monitored continuously; however, its interpretation was treated more cautiously because the cleaned time series frequently reached the upper analytical threshold adopted for supplementary visualization (2000 ppm). Therefore, CO_2 telemetry was retained as a monitored contextual variable rather than the primary basis for inferring environmental stability between the Constant and Gaussian windows; these complementary analyses are presented in Supplementary Section S8.

Regarding the energy–production relationship, the Constant profile showed lower SEC and higher EEMS than the Gaussian profile under RBW, blue, and red light (Fig. 4F; Table 1), whereas under white light there was no significant between-profile difference in SEC. Moreover, Areal Energy Consumption (AEC) was higher in the Gaussian profile for all spectra (Table 1), suggesting a higher electrical cost to deliver the protocol despite DLI equivalence. These results are consistent with two complementary factors, particularly under white light: (i) modulation may increase the fraction of time spent in states of higher photoprotective demand, reducing effective photosynthetic efficiency over the day, and (ii) modulation may shift the electrical operating point of the driver–LED system, affecting the wall-plug efficiency and the real cost per delivered photon [4,14,16].

Although the present study did not include a natural-light or conventional cultivation control, this omission should be interpreted in light of the study scope. The objective here was not to compare PFAL production directly against open-field or greenhouse systems, but rather to benchmark alternative lighting strategies within the same instrumented PFAL platform under controlled and auditable conditions. This distinction is important because broader literature indicates that PFAL and vertical-farming systems are substantially more electricity-dependent than greenhouse or open-field cultivation, while benchmarking itself remains a major challenge in the sector [5,45]. Therefore, the SEC and EEMS values reported here should be interpreted as within-system performance indicators for dynamic lighting management in PFALs, rather than as absolute evidence of superiority over conventional cultivation. Future studies should extend this comparison to daylight-assisted greenhouse or conventional references under harmonized crop, yield, and system-boundary criteria.

PSII photochemistry indicated that between-profile differences were most evident under white light: in the Constant profile, $Y(II)$ and q_P were higher and NPQ was lower, whereas in the Gaussian profile NPQ increased (Fig. 4B,C,E); ETR differed between profiles only under white light (Fig. 4D). However, energy cost per unit of biomass was not explained by instantaneous PSII variables: SEC correlated strongly with TMD ($r = -0.78$) and moderately with biomass traits, but showed weak correlations with NPQ, q_P, and ETR (Fig. 7). Thus, energy performance was dominated by time-integrated outcomes (harvested biomass) and by the effective electrical consumption of the protocol.

Across spectra, red light under the Constant profile was the most efficient energy–production combination, showing the lowest SEC (0.0998 kWh g^{-1}) and highest EEMS (10.02 g kWh^{-1}), consistent with higher dry mass yield per area (MSA) (Table 1) and greater dry biomass traits (Figure 5E–G). This pattern is mechanistically consistent with two complementary factors. First, red-centric horticultural lighting can achieve favorable photon efficacy, and dedicated 660 nm LED panels measured under plant-growth conditions have been reported to deliver higher photon efficacy than several white LED panels [4,44]. Second, red photons coincide with a major chlorophyll absorption region and can support biomass accumulation efficiently when daily light delivery is stable, a tendency also consistent with previous microgreen evidence under constant red lighting [6]. At the same time, this interpretation should be kept appropriately cautious: the present study did not directly measure the real-time relationship between delivered PPFD and electrical power consumption for each treatment (i.e., treatment-specific μmol J^{-1}), nor did it isolate luminaire-level wall-plug efficiency as an independent response variable. Therefore, the explanation for the superior Red–Constant performance should be interpreted as literature-consistent and mechanistically plausible, rather than as a direct demonstration of treatment-specific photon efficacy in the present experiment. In contrast, white light exhibited the highest SEC in both profiles and the lowest EEMS, indicating the highest energy cost per unit of dry biomass (Table 1).

Pigments exhibited a *profile* × *spectrum* interaction (Fig. 3). In the Constant profile, *Chla* was higher under white, RBW, and blue, whereas under red light, *Chla* was higher in the Gaussian profile. Carotenoids increased in the Gaussian profile under white, RBW, and red, and *Chlb* was higher in the Gaussian profile under white and red. Under RBW, *Chlb* was higher in the Constant profile, whereas under blue there was no difference between profiles (Fig. 3B). The *Chla*:*Chlb* ratio was higher in the Constant profile under white, RBW, and red, with no difference under blue. Taken together, these patterns suggest spectrum-dependent adjustments in light harvesting and photoprotection, with signals of greater photoprotective investment under modulation in specific conditions (e.g., white) [7,16].

Regarding growth traits, the Constant profile increased dry biomass (LMD, HMD, and TMD) under RBW, blue, and red and increased HFW for most spectra (except RBW), consistent with the lower SEC and higher EEMS observed in those combinations (Fig. 5; Table 1). Under white light, the Gaussian profile increased LFW (Fig. 5D), and TMD did not differ between profiles, offering no advantage in SEC/EEMS (Table 1). In microgreens, this decoupling is relevant because fresh mass may reflect expansion/hydration, whereas dry mass represents effective matter accumulation [17,18].

PCA reinforced the separation between energy performance and instantaneous variables: SEC loaded strongly on PC2 ($r = -0.76$), opposite to biomass variables, whereas PC1 contrasted biomass variables and NPQ (negative scores) with photochemical performance ($Y(II)$, q_P, and ETR; positive scores) (Fig. 6; Table 2). This supports the interpretation that SEC/EEMS better synthesize the trade-off between electrical cost and production than point-in-time PSII measurements.

As a limitation, the present conclusions are based on a single photoperiod, a specific daily light dose range, and a short cultivation cycle typical of sesame microgreens. Therefore, the relative performance of Constant and Gaussian light delivery should be interpreted within this experimental scope and not automatically extrapolated to longer crop cycles, other developmental stages, different DLI and photoperiod combinations, or other crop species [17]. Because plant responses to temporal light distribution can vary with canopy development, biomass accumulation, and source–sink dynamics over time, future studies should test these lighting strategies across broader phenological stages and under multiple DLI levels and photoperiod regimes.

In summary, the PVFS enabled auditable execution and verification of dynamic lighting protocols under controlled DLI, providing a robust basis for energy benchmarking in PFAL research. Within this experimental scope, the Constant profile improved energy–biomass efficiency under RBW, blue, and red light, and the Red–Constant treatment was the most efficient strategy (lowest SEC and highest EEMS), whereas white light incurred the highest energy cost per unit biomass (Table 1).

5. Conclusion

This study demonstrates that the *Precision Vertical Farming System* (PVFS) enables the reproducible execution and auditing of lighting protocols in PFALs by integrating (i) programmable temporal profiles under a target DLI, (ii) near real-time environmental and electrical telemetry, and (iii) an analytical *pipeline* (ANOVA/Tukey and PCA) to relate physiological and production responses to energy costs. Telemetry-based validation confirmed high sampling regularity and data completeness, verified DLI equivalence derived from recorded PPFD, and demonstrated the strong adherence of the Gaussian profile to its modeled shape, thereby minimizing operational uncertainty during treatment comparison.

Under a fixed photoperiod (12 h) and equivalent DLI (~ 10.8 mol m^{-2} d^{-1}), the temporal shape of PPFD delivery significantly influenced the energy–biomass trade-off in sesame microgreens. The Constant profile achieved superior energy-to-mass efficiency (lower SEC and higher EEMS) under RBW, blue, and red light, whereas the Gaussian profile increased Areal Energy Consumption (AEC) across all spectra. Among the evaluated treatments, the Red–Constant combination proved to be the most energy-efficient strategy, yielding the highest dry mass per unit of consumed energy, whereas white light exhibited the

highest energy cost per unit biomass. Multivariate analysis confirmed that SEC and EEMS aligned primarily with integrated biomass variables, reinforcing the conclusion that energy–production metrics capture operational system performance more effectively than instantaneous PSII photochemical measurements.

In terms of future perspectives, the PVFS provides a robust technical foundation for energy benchmarking and multi-objective optimization of lighting protocols. The system is extensible to experiments spanning multiple DLI levels, photoperiods, planting densities, and developmental stages, and supports integration with experimental planning routines, operational diagnostics, and the automated benchmarking of light "recipes" in dynamic scenarios.

Glossary / Abbreviations

PVFS: Precision Vertical Farming System: Open-architecture layered platform that executes lighting protocols and logs environmental/electrical telemetry for auditable, reproducible PFAL experiments.
PFAL: Plant Factory with Artificial Lighting: Indoor cultivation system in which artificial lighting is the primary driver of photosynthesis and production.
CEA: Controlled-Environment Agriculture: Production under controlled conditions (e.g., temperature, humidity, CO_2, and lighting), typically indoors.
PPFD: Photosynthetic Photon Flux Density (μmol m^{-2} s^{-1}): Photon flux (400–700 nm) incident on the crop canopy; used here as the time-varying lighting setpoint.
DLI: Daily Light Integral (mol m^{-2} d^{-1}): Time integral of PPFD over the photoperiod; used as the target daily light dose (equalized across treatments).
Constant profile: PPFD delivery with approximately constant intensity over the photoperiod (flat setpoint).
Gaussian profile: PPFD delivery described by a Gaussian-shaped curve over the photoperiod; compliance can be evaluated by goodness-of-fit metrics (e.g., R^2, RMSE).
RBW: Combined spectrum consisting of red, blue, and white components (reported proportions: 70.5% red, 21.0% blue, and 8.5% green from the white channel).
IoT: Internet of Things: Networked sensors/actuators enabling near real-time measurement (telemetry) and control in the growth chamber.
Telemetry: Time-stamped operational measurements (e.g., environmental variables, power/energy, and lighting control signals) transmitted and persisted for auditability and time-series analysis.
MQTT: Message Queuing Telemetry Transport: Lightweight publish/subscribe protocol used for device–server communication (telemetry and control).
JSON: JavaScript Object Notation: Structured payload format used to transmit messages (e.g., identifier, timestamp, metric, value, unit, status).
UTC: Coordinated Universal Time: Reference time zone used to timestamp telemetry records for traceability and comparability.
ISO-8601: International date-time format used for telemetry timestamps (e.g., 2024-03-08T12:00:00Z).
MongoDB: Document-oriented database used to persist raw telemetry records (with UTC timestamps) and support time-series queries/aggregations.
Docker / Docker Compose: Container-based deployment used to run infrastructure services with persistent volumes and version-controlled configurations.
ESP32: Wi-Fi-enabled microcontroller used as the embedded controller to acquire sensor data and apply lighting setpoints.
FreeRTOS: Real-time operating system supporting non-blocking embedded acquisition/control routines.
NTP: Network Time Protocol: Used for time synchronization, with RTC failover to increase tolerance to outages.
RTC: Real-Time Clock: Local clock module supporting timekeeping during connectivity/power interruptions.
DS3231: RTC module (I^2C) used for time synchronization/failover.
DAC: Digital-to-Analog Converter: Used to generate analog dimming signals for lighting control.
MCP4725: 12-bit I^2C DAC used to control LED driver dimming/PPFD output.
DHT22: Digital temperature/humidity sensor used in the chamber.
MH-Z14: NDIR CO_2 sensor used to measure CO_2 concentration in the chamber.
kWh: Kilowatt-hour: Energy unit used to quantify total electrical consumption during each treatment.
Power factor: Ratio of real to apparent power, used to characterize electrical load behavior.
AEC: Areal Energy Consumption (kWh m^{-2}): Total electrical energy consumed normalized by illuminated area.
MSA: Dry mass yield per area (g m^{-2}), estimated from mean dry mass per seedling and seedling density.
SEC: Specific Energy Consumption (kWh g^{-1}): Energy cost per gram of dry mass produced, computed as SEC = AEC/MSA.
EEMS: Energy-to-Mass Efficiency (g kWh^{-1}): Dry-mass return per unit of energy, defined as EEMS = 1/SEC.
REST: Representational State Transfer: API endpoints used for queries and control-service integration.
WebSocket: Bidirectional communication channel used for near real-time queries/notifications.
ANOVA: Analysis of Variance: Statistical framework used to test factor and interaction effects in the factorial design.
Tukey HSD: Tukey Honestly Significant Difference: Post-hoc multiple-comparison test used after ANOVA.
CLD: Compact Letter Display: Letter-based grouping that summarizes Tukey HSD results; groups sharing a letter are not significantly different at $\alpha = 0.05$.
PCA: Principal Component Analysis: Multivariate method used to summarize covariance structure and relate energy-performance metrics (SEC/EEMS) to dry-mass and photosynthetic variables.
TOST: Two One-Sided Tests: Equivalence testing applied to daily DLI values; equivalence margin defined as $\Delta = \pm 5\%$ around the target DLI using a 90% CI criterion.
CI: Confidence interval: Interval estimate used in inference and equivalence testing (e.g., 90% CI in TOST).
CV: Coefficient of variation (%): Relative dispersion measure, used e.g. to evaluate inter-channel uniformity.
R^2: Coefficient of determination: Goodness-of-fit metric for Gaussian-model compliance.
RMSE: Root mean square error (PPFD units): Fit error metric used to quantify Gaussian-model compliance.
MAE: Mean absolute error (PPFD units): Fit error metric used alongside RMSE.
IQR: Interquartile range: Robust dispersion metric used to guide winsorization.
Winsorization: Robust preprocessing replacing extreme values based on a rule (here, IQR-based) to reduce undue influence while preserving sample size.
PAM fluorometry: Pulse-amplitude modulated fluorometry used to obtain chlorophyll *a* fluorescence parameters with an IMAGING-PAM fluorometer.
Fo: Minimal fluorescence measured after dark adaptation under weak measuring light.
Fm: Maximal fluorescence induced by a saturating pulse after dark adaptation.
Fv/Fm: Maximum quantum yield of PSII, computed as $(F_m - F_o)/F_m$.
Y(II): Effective quantum yield of PSII under actinic light (light-adapted conditions).
NPQ: Non-photochemical quenching: Fluorescence-derived indicator of energy dissipation as heat under light-adapted conditions.
qP: Photochemical quenching coefficient under light-adapted conditions.
ETR: Electron transport rate, estimated as $\mathrm{ETR} = \mathrm{Y(II)} \times \mathrm{PAR} \times A_{\mathrm{leaf}} \times 0.5$.
PAR: Photosynthetically active radiation term used in ETR estimation.
A_{leaf}: Fraction of incident radiation absorbed by leaves; used in ETR calculation.

Funding

The author(s) declare that financial support was received for the research, authorship, and/or publication of this article. This project was funded by the National Council for Scientific and Technological Development (CNPq; Grant Nos. #408285/2021-4, #421052/2023-6, and #153369/2023-0) and by the Funding Authority for Studies and Projects/Research Support Foundation of the State of Goiás (FINEP/FAPEG; Tecnova II Grant No. #202010267000346).

Declaration of generative AI and AI-assisted technologies in the writing process

During the preparation of this work, the authors used ChatGPT to improve language clarity and readability. After using this tool, the authors reviewed and edited the content as needed and take full responsibility for the content of the publication.

CRediT authorship contribution statement

Marlus Dias Silva: Writing – review & editing, Writing – original draft, Visualization, Validation, Software, Methodology, Formal analysis, Data curation, Conceptualization; **Jaqueline Martins Vasconcelos:** Writing – review & editing, Supervision, Resources, Project administration, Methodology, Investigation; **Fábia Barbosa da Silva:** Writing – review & editing, Supervision, Project administration, Methodology, Funding acquisition, Conceptualization; **Adriano Soares de Oliveira Bailão:** Writing – review & editing, Validation, Software, Methodology; **Ítalo Moraes Rocha Guedes:** Writing – review & editing, Visualization, Methodology, Formal analysis, Data curation; **Márcio da Silva Vilela:** Writing – review & editing, Supervision, Resources; **Adriano Carvalho Costa:** Writing – review & editing, Supervision, Resources; **Márcio Rosa:** Writing – review & editing, Supervision, Resources; **Lucas Loram Lourenço:** Writing – review & editing, Investigation, Data curation; **Fabiano Guimarães Silva:** Writing – review & editing, Supervision, Project administration, Methodology, Funding acquisition, Conceptualization.

Data availability

The data generated and analyzed in this study are publicly available. The source code used in this study is available in the GitHub repository: https://github.com/marlussilva/pvfs-sesame-microgreens-cea.

Declaration of competing interest

The authors declare the following financial interests/personal relationships which may be considered as potential competing interests: Fabiano Guimaraes Silva reports financial support was provided by Goiano Federal Institute. If there are other authors, they declare that they have no known competing financial interests or personal relationships that could have appeared to influence the work reported in this paper.

Acknowledgments

The authors thank the Goiano Federal Institute of Education, Science and Technology - Rio Verde CAMPUS, the Pro-Rectory of Research, Postgraduate Studies, and Innovation of the Goiano Federal Institute, the National Council for Scientific and Technological Development (CNPq), and the Financier of Studies and Projects (FINEP), as well as the Research Support Foundation of the State of Goiás (FAPEG) for the funding.

Supplementary material

Supplementary material associated with this article can be found in the online version at 10.1016/j.atech.2026.102105.

References

[1] S.R. Jaeger, Vertical farming (plant factory with artificial lighting) and its produce: consumer insights, Curr. Opin. Food Sci. 56 (2024) 101145. https://doi.org/10.1016/j.cofs.2024.101145
[2] S. Oh, C. Lu, Vertical farming: smart urban agriculture for enhancing resilience and sustainability in food security, J. Hortic. Sci. Biotechnol. 98 (2) (2023) 133–140. https://doi.org/10.1080/14620316.2022.2141666
[3] M. Guo, Z. Jin, L. Ma, S. Ou, Application of plant factory with artificial lighting in horticultural production: current progress and future trends, Hortic. Plant J. (2025). https://doi.org/10.1016/j.hpj.2025.04.005
[4] P. Kusuma, P.M. Pattison, B. Bugbee, From physics to fixtures to food: current and potential LED efficacy, Hortic. Res. 7 (1) (2020) 56. https://doi.org/10.1038/s41438-020-0283-7
[5] L. Miserocchi, A. Franco, Benchmarking energy efficiency in vertical farming: status and prospects, Therm. Sci. Eng. Prog. 58 (2025) 103165. https://doi.org/10.1016/j.tsep.2024.103165
[6] M.D. Silva, J.M. Vasconcelos, F.B. da Silva, A.S. de Oliveira Bailão, Í.M.R. Guedes, M. da Silva Vilela, A.C. Costa, M. Rosa, F.G. Silva, Growing in red: impact of different light spectra and lighting conditions on lentil microgreens growth in vertical farming, Front. Plant Sci. 15 (2024). https://doi.org/10.3389/fpls.2024.1515457
[7] K.R. Susilo, A. Eu, B. Besemer, E. Heuvelink, R.C.H. de Vos, L.F.M. Marcelis, Extended photoperiod improves growth and nutritional quality of pak choi under constant daily light integral, Front. Plant Sci. 16 (2025). https://doi.org/10.3389/fpls.2025.1621513
[8] L.F. Lozano-Castellanos, L.M. Navas-Gracia, I.C. Lozano-Castellanos, A. Correa-Guimaraes, Technologies applied to artificial lighting in indoor agriculture: a review, Sustainability 17 (7) (2025) 3196. https://doi.org/10.3390/su17073196
[9] T. Miller, G. Mikiciuk, I. Durlik, M. Mikiciuk, A. Łobodzińska, M. Śnieg, The IoT and AI in agriculture: the time is now–A systematic review of smart sensing technologies, Sensors 25 (12) (2025). https://doi.org/10.3390/s25123583
[10] V.H.U. Eze, E.C. Eze, G.U. Alaneme, P.E. Bubu, E.O.E. Nnadi, M.B. Okon, Integrating IoT sensors and machine learning for sustainable precision agroecology: enhancing crop resilience and resource efficiency through data-driven strategies, challenges, and future prospects, Discov. Agric. 3 (1) (2025) 83. https://doi.org/10.1007/s44279-025-00247-y
[11] V. Choudhary, P. Guha, G. Pau, S. Mishra, An overview of smart agriculture using internet of things (IoT) and web services, Environ. Sustain. Indic. 26 (2025) 100607. https://doi.org/10.1016/j.indic.2025.100607
[12] Z. Wei, W. Fang, UV-NDVI for real-time crop health monitoring in vertical farms, Smart Agric. Technol. 8 (2024) 100462. https://doi.org/10.1016/j.atech.2024.100462
[13] M. Landolfo, F. Perotti, A. Pistillo, G. Pennisi, G. Gianquinto, F. Orsini, Optimizing artificial lighting for convolutional neural network-based crop monitoring with low-cost RGB imaging in indoor cultivation, Smart Agric. Technol. 13 (2026) 101677. https://doi.org/10.1016/j.atech.2025.101677
[14] N. Grasso, B. Fasciolo, G. Bruno, P. Chiabert, Development of a dynamic protocol for improving the productivity of soilless farming systems, Smart Agric. Technol. 12 (2025) 101264. https://doi.org/10.1016/j.atech.2025.101264
[15] J. Morales-Guerra, S. Suarez-Cortez, J. Morales-Duran, E. Reyes-Vera, J. Botero-Valencia, SmartGrow datacontrol: an IoT architecture for the acquisition of environmental physiological parameters in Cannabis sativa cultivations, SoftwareX 27 (2024) 101880. https://doi.org/10.1016/j.softx.2024.101880
[16] Kaiser, et al., Vertical farming goes dynamic, Front. Sci. 2 (2024) 1411259. https://doi.org/10.3389/fsci.2024.1411259
[17] J.K. Lone, R. Pandey, Gayacharan, Microgreens on the rise: expanding our horizons from farm to fork, Heliyon 10 (4) (2024) e25870. https://doi.org/10.1016/j.heliyon.2024.e25870
[18] M. Bhaswant, D.K. Shanmugam, T. Miyazawa, C. Abe, T. Miyazawa, Microgreens-A comprehensive review of bioactive molecules and health benefits, Molecules 28 (2) (2023) 867. https://doi.org/10.3390/molecules28020867
[19] E.R. Turner, Y. Luo, R.L. Buchanan, Microgreen nutrition, food safety, and shelf life: a review, J. Food Sci. (2020). https://doi.org/10.1111/1750-3841.15049
[20] Y. Fuji, A. Uchida, K. Fukahori, M. Chino, T. Ohtsuki, H. Matsufuji, Chemical characterization and biological activity in young sesame leaves (Sesamum indicum L.) and changes in iridoid and polyphenol content at different growth stages, PLOS ONE 13 (3) (2018) e0194449. https://doi.org/10.1371/journal.pone.0194449
[21] T. Domínguez-Bolaño, O. Campos, V. Barral, C.J. Escudero, J.A. García-Naya, An overview of IoT architectures, technologies, and existing open-source projects, Internet Things 20 (2022) 100626. https://doi.org/10.1016/j.iot.2022.100626
[22] H. Mrabet, S. Belguith, A. Alhomoud, A. Jemai, A survey of IoT security based on a layered architecture of sensing and data analysis, Sensors 20 (13) (2020) 3625. https://doi.org/10.3390/s20133625
[23] R. Gong, H. Zhang, G. Li, J. He, Edge computing-enabled smart agriculture: technical architectures, practical evolution, and bottleneck breakthroughs, Sensors 25 (17) (2025) 5302. https://doi.org/10.3390/s25175302
[24] P. Yu, F. Teng, W. Zhu, C. Shen, Z. Chen, J. Song, Cloud–edge–device collaborative computing in smart agriculture: architectures, applications, and future perspectives, Front. Plant Sci. 16 (2025) 1668545. https://doi.org/10.3389/fpls.2025.1668545
[25] J. Wytrębowicz, K. Cabaj, J. Krawiec, Messaging protocols for IoT systems–A pragmatic comparison, Sensors 21 (20) (2021) 6904. https://doi.org/10.3390/s21206904
[26] D. Silva, L.I. Carvalho, J. Soares, R.C. Sofia, A performance analysis of internet of things networking protocols: evaluating MQTT, CoAP, OPC UA, Appl. Sci. 11 (11) (2021) 4879. https://doi.org/10.3390/app11114879
[27] A. Larmo, A. Ratilainen, J. Saarinen, Impact of CoAP and MQTT on NB-IoT system performance, Sensors 19 (1) (2019) 7. https://doi.org/10.3390/s19010007
[28] J. Martin, J. Burbank, W. Kasch, D.L. Mills, Network time protocol version 4: protocol and algorithms specification, 2010, (RFC 5905). https://doi.org/10.17487/RFC5905
[29] I. Fette, A. Melnikov, The WebSocket protocol, 2011, (RFC 6455). https://doi.org/10.17487/RFC6455
[30] C.A. Schneider, W.S. Rasband, K.W. Eliceiri, NIH Image to ImageJ: 25 years of image analysis, Nat. Methods 9 (7) (2012) 671–675. https://doi.org/10.1038/nmeth.2089
[31] B. Genty, J.-M. Briantais, N.R. Baker, The relationship between the quantum yield of photosynthetic electron transport and quenching of chlorophyll fluorescence, Biochim. Biophys. Acta - Gen. Subj. 990 (1) (1989) 87–92. https://doi.org/10.1016/S0304-4165(89)80016-9
[32] T. Lawson, D.M. Kramer, C.A. Raines, Improving yield by exploiting mechanisms underlying natural variation of photosynthesis, Curr. Opin. Biotechnol. 23 (2) (2012) 215–220. https://doi.org/10.1016/j.copbio.2011.12.012

[33] W. Bilger, U. Schreiber, M. Bock, Determination of the quantum efficiency of photosystem II and of non-photochemical quenching of chlorophyll fluorescence in the field, Oecologia 102 (4) (1995) 425–432. https://doi.org/10.1007/BF00341354
[34] A. Laisk, F. Loreto, Determining photosynthetic parameters from leaf CO2 exchange and chlorophyll fluorescence (Ribulose-1,5-Bisphosphate carboxylase/oxygenase specificity factor, dark respiration in the light, excitation distribution between photosystems, alternative electron transport rate, and mesophyll diffusion resistance), Plant Physiol. 110 (3) (1996) 903–912. https://doi.org/10.1104/pp.110.3.903
[35] J.N. de Castro, C. Müller, G.M. Almeida, A.C. Costa, Physiological tolerance to drought under high temperature in soybean cultivars, Aust. J. Crop Sci. 13 (2019) 976–987. https://doi.org/10.21475/AJCS.19.13.06.P1767
[36] A.R. Wellburn, The spectral determination of chlorophylls a and b, as well as total carotenoids, using various solvents with spectrophotometers of different resolution, J. Plant Physiol. 144 (3) (1994) 307–313. https://doi.org/10.1016/S0176-1617(11)81192-2
[37] H. Kyauk, N.W. Hopper, R.D. Brigham, Effects of temperature and presoaking on germination, root length and shoot length of sesame (Sesamum indicum L.), Environ. Exp. Bot. 35 (3) (1995) 345–351. https://doi.org/10.1016/0098-8472(95)00013-X
[38] H. Balouchi, V.S. Khankahdani, A. Moradi, M. Gholamhoseini, R. Piri, S.Z. Heydari, B. Dedicova, Seed fatty acid changes germination response to temperature and water potentials in six sesame (Sesamum indicum L.) cultivars: estimating the cardinal temperatures, Agriculture 13 (10) (2023) 1936. https://doi.org/10.3390/agriculture13101936
[39] G. Parmoon, S.A. Moosavi, A. Poshtdar, S.A. Siadat, Effects of cadmium toxicity on sesame seed germination explained by various nonlinear growth models, Ocl 27 (2020) 57. https://doi.org/10.1051/ocl/2020053
[40] D. Lakens, Equivalence tests: a practical primer for t tests, correlations, and meta-analyses, Soc. Psychol. Personal. Sci. (2017). Open access (PMC), https://doi.org/10.1177/1948550617697177
[41] W. Du, P. Jin, W. Jin, Smart farm digital twin model based on edge-cloud architecture for tomato monitoring and detection, Smart Agric. Technol. 12 (2025) 101254. https://doi.org/10.1016/j.atech.2025.101254
[42] A.S. Rathor, S. Choudhury, A. Sharma, P. Nautiyal, G. Shah, Empowering vertical farming through IoT and AI-Driven technologies: a comprehensive review, Heliyon 10 (15) (2024) e34998. https://doi.org/10.1016/j.heliyon.2024.e34998
[43] L.-D. Van, Y.-B. Lin, T.-H. Wu, Y.-W. Lin, S.-R. Peng, L.-H. Kao, C.-H. Chang, PlantTalk: a smartphone-based intelligent hydroponic plant box, Sensors 19 (8) (2019) 1763. https://doi.org/10.3390/s19081763
[44] T.I. Wong, X. Zhou, Photon efficacy and cost investigation of LEDs at different wavelengths and color temperatures for horticulture, Discov. Agric. 2 (2024) 125. https://doi.org/10.1007/s44279-024-00137-9
[45] C. Stanghellini, D. Katzin, The dark side of lighting: a critical analysis of vertical farms' environmental impact, J. Clean. Prod. 458 (2024) 142359. https://doi.org/10.1016/j.jclepro.2024.142359
[46] H. Liu, F. Zhou, T. Zhou, Y. Yang, Y. Zhao, A novel wrinkled-leaf sesame mutant as a potential edible leafy vegetable rich in nutrients, Sci. Rep. 12 (2022) 18478. https://doi.org/10.1038/s41598-022-23263-0
[47] K.P. Gavhane, M. Hasan, D.K. Singh, et al., Determination of optimal daily light integral (DLI) for indoor cultivation of iceberg lettuce in an indigenous vertical hydroponic system, Sci. Rep. 13 (2023) 10923. https://doi.org/10.1038/s41598-023-36997-2
[48] G. Alturif, W. Saleh, A.A. El-Bary, R.A. Osman, Towards efficient IoT communication for smart agriculture: a deep learning framework, PLOS ONE (2024). https://doi.org/10.1371/journal.pone.0311601
[49] N. Kharraz, A. Revoly, I. Szabó, IoT-based adaptive lighting framework for optimizing energy efficiency and crop yield in indoor farming, J. Sens. Actuator Netw. 14 (3) (2025) 59. https://doi.org/10.3390/jsan14030059
[50] N. Kharraz, I. Szabó, Cloud-driven data analytics for growing plants indoor, AgriEngineering 7 (4) (2025) 101. https://doi.org/10.3390/agriengineering7040101
[51] K. Dineva, T. Atanasova, Cloud data-driven intelligent monitoring system for interactive smart farming, Sensors 22 (17) (2022) 6566. https://doi.org/10.3390/s22176566
[52] V. Wichitwechkarn, W. Rohde, R. Choudhary, Design and validation of an open-sourced automation system for vertical farming, HardwareX 16 (2023) e00497. https://doi.org/10.1016/j.ohx.2023.e00497
[53] N.N. Thilakarathne, M.S. Abu Bakar, P.E. Abas, H. Yassin, Towards making the fields talks: a real-time cloud enabled IoT crop management platform for smart agriculture, Front. Plant Sci. 13 (2023). https://doi.org/10.3389/fpls.2022.1030168